Monthly Notices
of the
ROYAL ASTRONOMICAL SOCIETY

MNRAS **529,** 4666–4680 (2024) https://doi.org/10.1093/mnras/stae848
Advance Access publication 2024 March 26

The progenitors of the intra-cluster light and intra-cluster globular clusters in galaxy groups and clusters

Niusha Ahvazi ,[1,2]★ Laura V. Sales ,[1] Jessica E. Doppel ,[1] Andrew Benson ,[2] Richard D'Souza [3] and Vicente Rodriguez-Gomez [4]

[1] *Department of Physics and Astronomy, University of California, Riverside, 900 University Avenue, Riverside, CA 92521, USA*
[2] *Carnegie Observatories, 813 Santa Barbara Street, Pasadena, CA 91101, USA*
[3] *Vatican Observatory, Specola Vaticana, V-00120, Vatican City State*
[4] *Instituto de Radioastronomía y Astrofísica, Universidad Nacional Autónoma de México, Apdo. Postal 72-3, 58089 Morelia, Mexico*

Accepted 2024 March 19. Received 2024 March 4; in original form 2023 August 22

ABSTRACT

We use the TNG50 from the IllustrisTNG suite of cosmological hydrodynamical simulation, complemented by a catalogue of tagged globular clusters, to investigate the properties and build up of two extended luminous components: the intra-cluster light (ICL) and the intra-cluster globular clusters (ICGCs). We select the 39 most massive groups and clusters in the box, spanning the range of virial masses $5 \times 10^{12} < \mathrm{M}_{200}/\mathrm{M}_{\odot} < 2 \times 10^{14}$. We find good agreement between predictions from the simulations and current observational estimates of the fraction of mass in the ICL and its radial extension. The stellar mass of the ICL is only ~ 10 per cent–20 per cent of the stellar mass in the central galaxy but encodes useful information on the assembly history of the group or cluster. About half the ICL in all our systems is brought in by galaxies in a narrow stellar mass range, $M_* = 10^{10}$–$10^{11}\ \mathrm{M}_{\odot}$. However, the contribution of low-mass galaxies ($M_* < 10^{10}\ \mathrm{M}_{\odot}$) to the build up of the ICL varies broadly from system to system, ~ 5 per cent $-$ 45 per cent, a feature that might be recovered from the observable properties of the ICL at $z = 0$. At fixed virial mass, systems where the accretion of dwarf galaxies plays an important role have shallower metallicity profiles, less metal content, and a lower stellar mass in the ICL than systems where the main contributors are more massive galaxies. We show that intra-cluster GCs are also good tracers of this history, representing a valuable alternative when diffuse light is not detectable.

Key words: galaxies: clusters: intracluster medium – globular clusters: general – galaxies: dwarf – galaxies: general.

1 INTRODUCTION

One of the most striking features of high-density environments is the intra-cluster light (ICL), a diffuse component of light that originates from populations of stars that are not associated with individual galaxies and are instead gravitationally bound to the host dark matter halo. The ICL is thought to be a product of the tidal stripping of stars from galaxies as they traverse the cluster or group environments and was first proposed and subsequently discovered by Zwicky (1937, 1951, 1952, 1957) in the Coma cluster. The direct link between the ICL and satellite galaxies makes the formation of this diffuse light a natural prediction of the hierarchical assembly model in Cold Dark Matter (CDM, White & Rees 1978; Conroy, Wechsler & Kravtsov 2007; Montes & Trujillo 2018; Contini 2021).

The ICL has cosmological relevance primarily in two aspects. First, it represents a visible tracer of the unseen dark matter distribution, with several theoretical works supporting a good correlation between the shape and orientation of the ICL and those of the underlying dark matter halo (Montes & Trujillo 2019; Alonso Asensio et al. 2020; Contini & Gu 2020; Deason et al. 2020; Gonzalez et al. 2021). Secondly, the main focus of this paper, the ICL is built by the tidal disruption of many satellite galaxies, some of which do not survive until today. As such it can help unravel the past formation history of the host group or cluster halo (Contini 2021; Montes 2022, and references therein), in a similar way that stellar haloes can help reconstruct the merger histories of smaller mass haloes in the Milky Way-like (MW-like) regime (e.g. Bullock & Johnston 2005).

The stellar mass content of the ICL is directly related to the stellar mass–halo mass relation and serves as a probe of the past assembly history of galaxy clusters. A number of observational constraints on the amount of ICL have been reported in the literature, with studies using deep imaging to estimate the total amount of ICL in galaxy clusters (e.g. Zibetti et al. 2005; Krick & Bernstein 2007; McGee & Balogh 2010; Mihos et al. 2017; Morishita et al. 2017; Jiménez-Teja et al. 2019a). These studies have found that the ICL typically makes up a significant fraction of the total light in galaxy clusters, ranging from <10 per cent to 50 per cent depending on the cluster and the methods used to estimate the ICL (see Montes 2022).

Numerical simulations predict that the bulk of the ICL mass comes from the tidal stripping of massive satellites ($10 < \log(\mathrm{M}/\mathrm{M}_{\odot}) < 11$) (Puchwein et al. 2010; Contini et al. 2013; Cui et al. 2014; Cooper et al. 2015; Contini, Yi & Kang 2019; Montenegro-Taborda

---

★ E-mail: niusha.ahvazi@email.ucr.edu

et al. 2023). Particularly, disc-like massive satellites are thought to significantly contribute to building the ICL through a large number of small stripping events (Contini et al. 2018). However, other less-dominant mechanisms may also contribute stars to the ICL including the total disruption of low mass satellites (Purcell, Bullock & Zentner 2007), stars ejected into the inter-cluster medium after a major merger (Murante et al. 2007) and the pre-processing of accreted groups (Rudick, Mihos & McBride 2006). Due to the well-established relation between stellar mass and metallicity in galaxies, the nature of the progenitors that build up the ICL can be observationally constrained from stellar metallicities. Furthermore, each of these mechanisms are expected to leave distinct patterns on the metallicity and their gradients.

Constraining the contribution of each mechanism can be extremely challenging due to the faint ($\mu_V \sim 26.5$ mag/arcsec^2) and extended characteristics of the ICL, which can often only be probed by broad-band photometry. Yet, over the last two decades, significant progress has been made. A number of observational studies have highlighted the presence of clear negative radial colour gradients (Krick & Bernstein 2007; Rudick et al. 2009; Melnick et al. 2012; DeMaio et al. 2015) in the ICL of the majority of clusters studied at $z \sim 0.5$. While such gradients could potentially arise due to changes in metallicity (Montes & Trujillo 2014; DeMaio et al. 2015) or variations in the ages of the stars (Morishita et al. 2017; Montes & Trujillo 2018), it suggests that violent relaxation after major mergers with the BCG cannot be the dominant source of ICL. Although, the observed metallicities of the ICL ($[\mathrm{Fe/H}]_{\mathrm{ICL}} \sim -0.5$) align with the notion that the ICL stars likely originate either from stars located in the outer regions of galaxies with stellar masses approximately $5 \times 10^{10}\,\mathrm{M}_\odot$ (DeMaio et al. 2018; Montes & Trujillo 2018; Montes et al. 2021) or from the dissolution of dwarf galaxies, the amount of ICL is often used as an argument against the latter as this would dramatically alter the faint end of the cluster galaxy luminosity function (e.g. Zibetti et al. 2005; DeMaio et al. 2018). Only a small number of clusters have been identified with flat colour gradients (e.g. Abell 370) – indicating an ICL formed through the expulsion of stars into the intra-cluster medium during a major merger event (Krick & Bernstein 2007; DeMaio et al. 2015, 2018). While the vast variety of observations point to the progenitors of the ICL being the tidal stripping of massive satellites ($10 < \log(\mathrm{M/M}_\odot) < 11$) consistent with theoretical predictions, the ICL of the two closest well-studied clusters, the Virgo and Coma, which can be studied in significant detail, suggest very different assembly mechanisms. Williams et al. (2007), studying the RGB populations of the Virgo cluster (~15 Mpc) using a single and deep *HST* pointing, found that 70 per cent of the stars have a metallicity of $[\mathrm{M/H}] \sim -1.3$) indicating that the ICL was built up primarily through the disruption of dwarf galaxies. Similarly, Gu et al. (2020) spectroscopically studied the ICL of the Coma cluster in the low-S/N regime finding it to be old and metal-poor ($[\mathrm{M/H}] \sim -1.0$) – consistent with the accretion of low-mass galaxies or the tidal stripping of the outskirts of massive galaxies that have ended their star formation early on. The low metallicity of the ICL of the Virgo and the Coma cluster clearly suggests that the contribution of dwarf galaxies to the ICL can be significant. This is clearly in tension with the observations of clusters further away as well as the current theoretical paradigm, requiring further study and perhaps a revision of understanding of the contribution of dwarf galaxies to the ICL.

One way to observationally disentangle the various formation mechanisms is to study how the ICL correlates with the mass of the cluster and with redshift. However, as we probe deeper into the universe and examine systems at earlier redshifts, the low-surface brightness of the ICL becomes increasingly difficult to capture. In such cases, an alternative path to study the dark matter haloes may be offered by globular clusters (GCs). These ancient, dense clusters of stars are commonly found in nearly all types of galaxies and are thought to be among the oldest and (often) metal-poor stellar populations in the universe (Gratton et al. 2019). They are believed to have formed before the majority of galaxies and are relatively luminous (Schauer et al. 2021), making them easily detectable at large distances and earlier redshifts and a powerful tool to study the distribution of dark matter and ICL in the early universe.

GCs can be very numerous in groups and clusters. While for MW-like galaxies they populate host haloes by the hundreds, in the Virgo cluster more than 10 000 have been catalogued around M87 (Durrell et al. 2014). Studies have shown that the abundance of GCs is closely related to the amount of dark matter in the haloes (Spitler & Forbes 2009; Harris, Harris & Alessi 2013; Hudson, Harris & Harris 2014; Harris, Harris & Hudson 2015). Therefore, GCs can offer an alternative path to study the dark matter haloes in galaxy groups and clusters, especially when the ICL is not easily captured.

A large fraction of GCs associated with a given system are members of the intra-cluster globular cluster (ICGC) component, which has been observationally confirmed in Fornax (Schuberth et al. 2008), Coma (Madrid et al. 2018), Abell 1689 (Alamo-Martínez & Blakeslee 2017), Virgo (Lee, Park & Hwang 2010; Ko et al. 2017; Longobardi et al. 2018), Centaurus A (Taylor et al. 2017), Perseus (Harris et al. 2020), and Abell 2744 (Harris & Reina-Campos 2023) for example. This intra-cluster component is expected to arise mostly by the gravitational removal of GCs from satellite galaxies that interacted with the groups, and pre-dominantly from satellites that did not survive until today (Ramos-Almendares et al. 2020). In this way, the origin of the ICGCs and the ICL are therefore expected to be strongly linked, and one might naively expect similar properties and building blocks for both components. However, the way stars and GCs occupy haloes is different, in particular in the low-mass end of dwarf galaxies, and it is as yet unclear how this may impact the way GCs and the ICL trace each other.

In this study, we take advantage of the recently published catalogue of GCs[1], which are tagged post-processing into the cosmological hydrodynamical simulation TNG50 to explore the properties of the ICL and GC components of groups and clusters. The paper is organized as follows: in Section 2, we present a brief description of the simulation and definitions used in our study. In Section 3, we introduce the general properties of the ICL component predicted by the simulation. In Section 4, we analyse the progenitors of the ICL component, and in Section 5, we investigate the use of GCs as tracers of the formation history of ICL. Finally, in Section 6, we summarize the main results of our study.

2 SIMULATION

We use the TNG50 of the IllustrisTNG suite of cosmological hydrodynamical simulation (Pillepich et al. 2019; Nelson et al. 2019b), which is part of the suite of cosmological boxes from the IllustrisTNG project[2] (Marinacci et al. 2018; Naiman et al. 2018; Nelson et al. 2018; Springel et al. 2018; Pillepich et al. 2018b; Nelson et al. 2019a). TNG50 is the highest resolution baryonic run of the IllustrisTNG suite, which has a volume of approximately 50^3 Mpc^3 and 2×2160^3 resolution elements, with an average mass per baryonic particle $8.5 \times 10^4\mathrm{M}_\odot$, and dark matter mass with $4.5 \times 10^5\mathrm{M}_\odot$ per

---

[1] https://www.tng-project.org/doppel22

[2] https://www.tng-project.org

particle. The IllustrisTNG cosmological parameters are consistent with ΛCDM model determined by Planck XIII (Planck Collaboration et al. 2016) to be $\Omega_{\mathrm{m}} = 0.3089$, $\Omega_{\mathrm{b}} = 0.0486$, $\Omega_{\Lambda} = 0.6911$, $H_0 = 100\,h$ km s^{-1} Mpc^{-1} with $h = 0.6774$, $\sigma_8 = 0.8159$, and $n_{\mathrm{s}} = 0.9667$.

The evolution of gravity and hydrodynamics are followed using the AREPO moving mesh code (Springel 2010). The galaxy formation baryonic treatment is based on its predecessor simulation suite, Illustris (Vogelsberger et al. 2013; Genel et al. 2014; Vogelsberger et al. 2014a, b; Nelson et al. 2015), with modifications implemented to better track the formation and evolution of galaxies, as described in Weinberger et al. (2017); Pillepich et al. (2018a).

The updated IllustrisTNG subgrid models accounts for star formation, radiative metal cooling, chemical enrichment from SNII, SNIa, and AGB stars, stellar feedback, and super-massive black hole feedback (Weinberger et al. 2017; Pillepich et al. 2018a). These models are shown to reproduce several of the $z = 0$ basic galaxy scaling relations, including the stellar mass – size (Genel et al. 2018), the colour bimodality (Nelson et al. 2018), and galaxy clustering (Springel et al. 2018), among others. As such, they are representative of the present-day population of galaxies in the universe and reproduce the main environmental trends observed in satellites. Of particular relevance to this work, the abundance of low-mass and intermediate-mass galaxies seems consistent with observationally estimated stellar mass functions (e.g. Pillepich et al. 2018a; Vázquez-Mata et al. 2020; Engler et al. 2021).

2.1 Identification of groups and clusters

Groups are identified using spatial information based on a Friends-of-Friends (FoF) algorithm (Davis et al. 1985). Individual self-gravitating subhaloes and galaxies are later found in these groups using SUBFIND (Springel et al. 2001; Dolag et al. 2009). The object at the centre of the gravitational potential of each group is called the 'central' galaxy, while all other substructures are 'satellites' (or 'subhaloes'). SUBFIND identifies substructures with a minimum of 32 particles and we additionally apply $\mathrm{M_{DM}} \geqslant 5.4 \times 10^7\ \mathrm{M_\odot}$ (at the time of infall) to remove the chances of including spurious baryonic clumps that are not bonafide galaxies. The time evolution of galaxies and haloes through the 99 snapshots of the simulation is followed by using the SUBLINK merger trees (Rodriguez-Gomez et al. 2015).

We identify groups and low-mass clusters in TNG50 by selecting all host haloes with virial masses $M_{200}/\mathrm{M_\odot} \geqslant 5 \times 10^{12}$, where virial quantities are measured within the virial radius, or r_{200}, defined as the radius of a sphere where the mean density of the group is 200 times the critical density of the universe. This selection results in 39 groups and clusters, containing 3305 and 5020 satellite galaxies with $M_* > 10^7\ \mathrm{M_\odot}$ within the virial radius and FoF group boundaries, respectively.

2.2 The ICL in groups and clusters

For the purpose of this work we define the ICL as all stellar particles that belong to the group and are not bound to any satellite, and are located within a radial range of $0.15\,\mathrm{r_{200}} < \mathrm{r} < \mathrm{r_{200}}$ from the host galaxy, where $\mathrm{r_{200}}$ is the virial radius of the group. Different definitions of ICL are commonly assumed in the literature, both in simulations and observational work. We have experimented with several of these definitions and explicitly checked that none of our main conclusions depends qualitatively on the specific criteria adopted here. For a more detailed view, we collect in Appendix A some examples on how the exact definition of ICL affects some of our reported results.

Further inspection of our selection of ICL particles revealed an excess of stars located on the periphery of several satellites. These stellar particles are considered unbound by SUBFIND (and therefore included as ICL candidates) but are still clearly part of the satellite or substructure in the 6D space of positions and velocities. We therefore applied two extra requirements in order to 'clean' our ICL sample. Each stellar particle needs to be at least $10 \times \mathrm{r_{h_*}}$ away from any massive satellite (the ones larger than $\mathrm{M/M_\odot} > 10^{10}$), where $\mathrm{r_{h_*}}$ is the stellar half-mass radius of the satellite. In addition, we ensure that the velocity of the particles satisfy $\mathrm{V/V_C} > 2.5$ to be considered part of the ICL, where $\mathrm{V_C}$ is the circular velocity at $2 \times \mathrm{r_{h_*}}$ of the satellite. This procedure satisfactorily removes extra stellar particles with positions and velocities strongly correlated with the local substructure. Note that similar methods are used in observations of the ICL to reduce the light contamination from the central galaxy and the satellite galaxies.

2.3 *In situ* versus ex situ

In this paper, we frequently use the terms '*in situ*' and 'ex-situ' to distinguish between different types of stellar populations: those born from gas bound to the main branch progenitor in the SUBLINK merger tree of a galaxy ('*in situ*') versus those born in external galaxies and later brought in to the descendant object during mergers or tidal stripping events ('ex-situ').

To classify stars as ex situ or *in situ*, we use the stellar assembly catalogues, offered as auxiliary data in the TNG data base. The classification method was introduced in detail in Rodriguez-Gomez et al. (2016) and is based on the SUBFIND association of the newly formed stars (at the time of birth) to either the main progenitor of the central galaxy (*in situ*) or to a substructure that later merges into the system (ex situ). Main or secondary progenitors are defined using the SUBLINK merger trees.

2.4 GCs

We use the catalogue of GCs presented in Doppel et al. (2023) for our TNG50 systems. GCs are tagged for all galaxies with $\mathrm{M_{*,max}} \geq 5 \times 10^6\ \mathrm{M_\odot}$ that infall or interact with our groups and clusters. The tagging is done at infall time for all galaxies, after which the dynamics of the GCs is followed naturally by tracking the positions and velocities of the particles flagged as GC candidates. The simulated GCs are shown to follow known scaling relations for galaxy-GCs and, in addition, to give rise to a population of intra-cluster GCs (ICGCs) as a combination of tidal stripping of GCs from merging galaxies and a native GC population tagged on to the central galaxy (Ramos-Almendares et al. 2020; Doppel et al. 2023). The slope and normalization of this ICGC component is in rough agreement with current observational constraints (see fig. 5 in Doppel et al. 2023). GCs are tagged to selected dark matter particles and are assigned masses $M_{\mathrm{GC}} = 7 \times 10^3$–$5 \times 10^6\ \mathrm{M_\odot}$ as described in more detail in Appendix B. For additional information we refer the reader to Doppel et al. (2023).

For this work, we use from this catalogue the ICGCs, identified as tagged GCs that are currently not associated to any substructure according to SUBFIND and 'cleaned' with the same method described in subsection 2.2 for the ICL. As an example of how these GCs are distributed in our systems, we show in Fig. 1, projected maps of multiple groups from our sample. These plots show the stellar component (grey-scale in the background) with the position of the

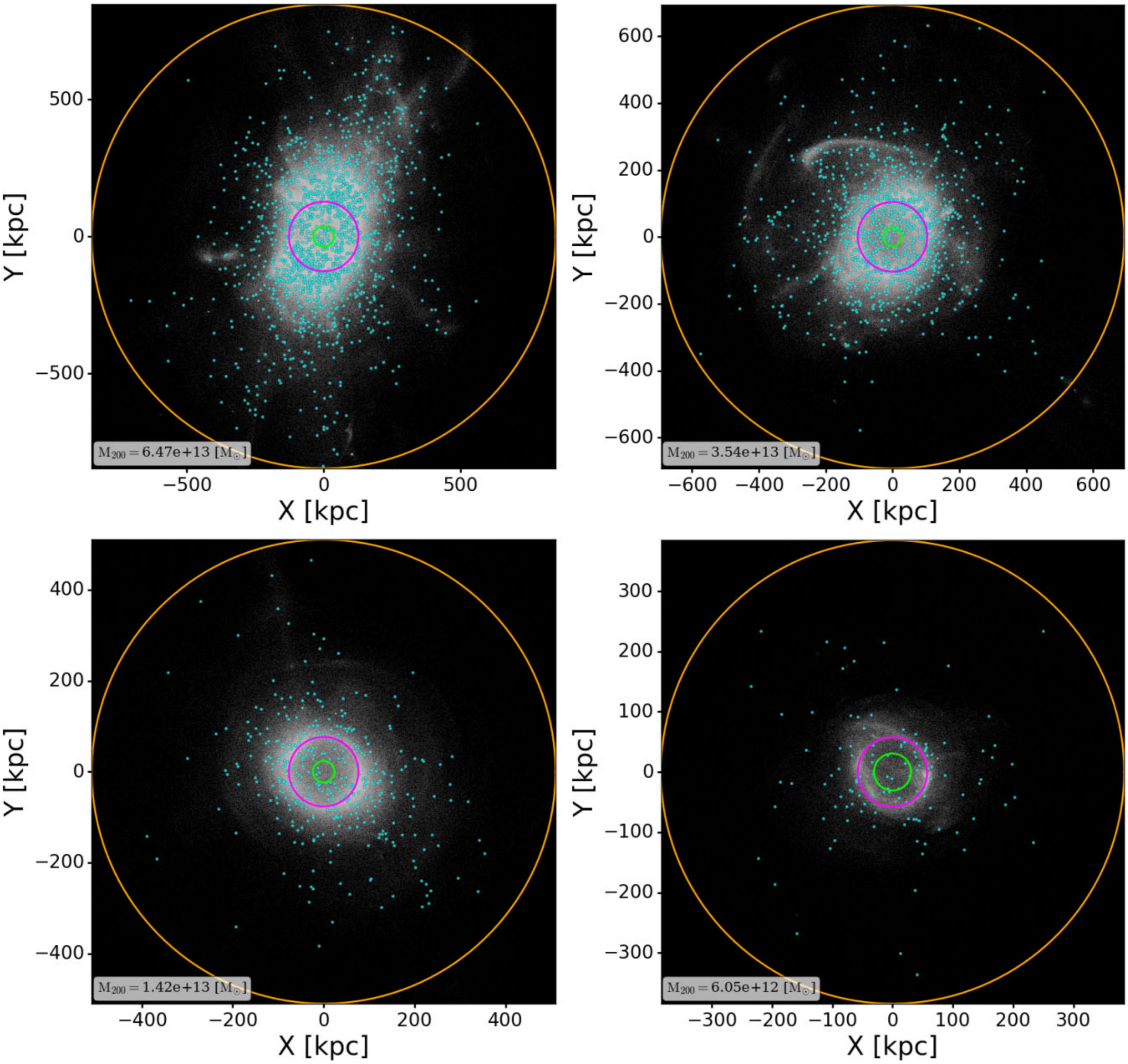

Figure 1. Projected position of the luminous (stellar (grey-scale background) + ICGCs (cyan dots)) components in the ICL of 4 randomly selected groups from our sample (the virial mass of each group is quoted on the bottom left of each panel). Orange, magenta, and lime circles show the position of r_{200} for the group, and $0.15 \times r_{200}$, and $2 \times r_{h_*}$, respectively.

ICGCs highlighted by the cyan dots. These few examples illustrate interesting differences in size, shapes, and concentration of the GC and ICL components, suggesting a link to their different formation histories.

3 THE MASS AND EXTENT PREDICTED FOR THE ICL

3.1 ICL mass content

In order to quantify the amount of mass in the ICL, we define the fraction of mass in the ICL as

$$f_{\rm ICL} = \frac{M^*_{ICL}}{M^*_{BCG}}, \tag{1}$$

where $M^*_{\rm ICL}$ is the stellar mass in the ICL and $M^*_{\rm BCG}$ is the stellar mass within $2 \times r_{h_*}$ of the central galaxy. Solid circles with black outlines in Fig. 2 show $f_{\rm ICL}$ for our sample of groups and clusters plotted against the virial mass of each group. We note that various definitions of this fraction have been used in the literature. In particular, a lower limit to $f_{\rm ICL}$ might be found by dividing the mass of the ICL by the total mass of stars within the virial radius $f_{\rm ICL,tot} = M_{\rm ICL}/M_{*,r_{200}}$. For comparison, we show $f_{\rm ICL,\,tot}$ in Fig. 2 with downward triangles connected to the solid symbols. In general, we find that the ICL fraction can change by more than a factor of two by adopting common definitions in the literature (see Appendix A). In this work, $f_{\rm ICL}$ will refer to equation (1) unless specified otherwise.

Our systems span from 5×10^{12} to nearly 2×10^{14} $M_\odot$ in virial mass, sampling the range from isolated elliptical galaxies comparable to Centaurus A to moderate mass galaxy clusters such as Fornax,

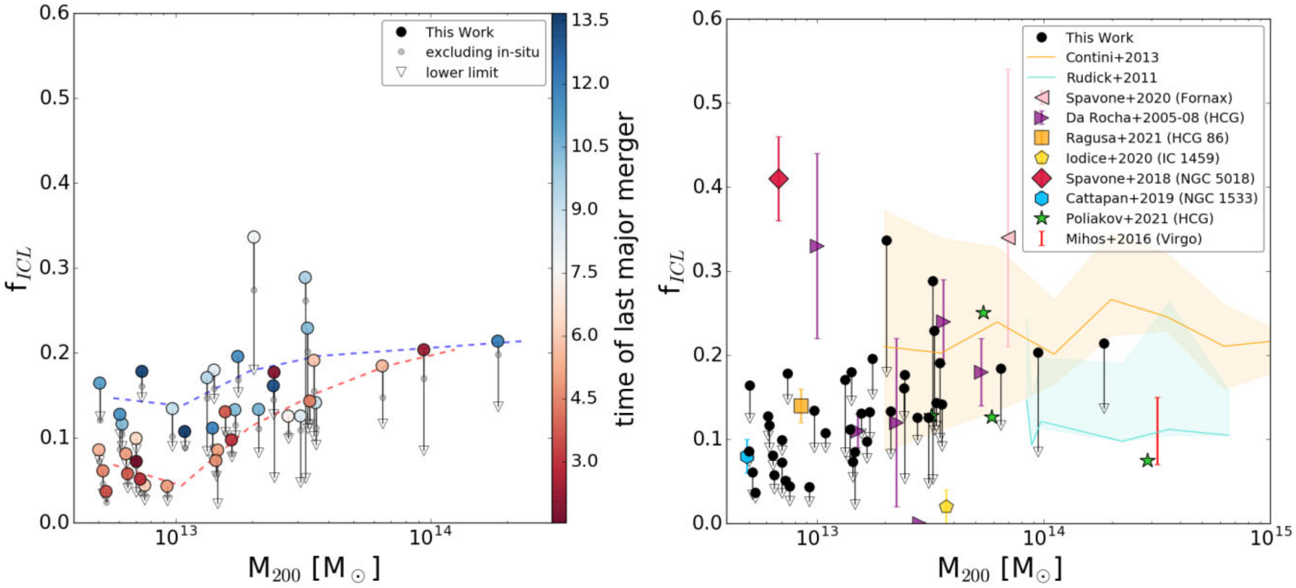

Figure 2. Left panel: ICL fraction as a function of virial mass of our groups and clusters colour codded by the time of the last major merger of the central galaxy. Predictions from TNG50 are shown with large filled circles (upper limit), and empty downward triangles (lower limit). Small grey circles indicate the fraction if only ex situ or accreted stars are considered. Right panel: Comparison of the predicted ICL fraction in TNG50 with results from previous simulations (shaded areas) and several observational studies (different markers). References along with the reported quantities are presented in Table D1 in Appendix D.

and conservative mass estimates of the Virgo cluster. The ICL mass fraction shows a subtle increase with virial mass, with typical values of 5–10 per cent in our low mass systems and ∼ 20 per cent for our more massive clusters. The relation also exhibits a substantial degree of dispersion at a given mass (results are comparable to the best fit relation in Ragusa et al. 2023, albeit with lower scatter).

We trace back the dispersion in this relation to the assembly history of each group. The colour coding in the left panel of Fig. 2 shows that, at fixed halo mass, groups with a longer time since their last major merger tend to show lower ICL mass fractions than groups where the last major merger was more recent. This trend has been quantified by categorizing the systems into ‘red’ and ‘blue’ groups, based on whether their last major merger occurred within 7.5 Gyr or after. Major mergers are here defined as merger events of the central galaxy with satellites of stellar mass ratios greater than 0.25 measured at the time of maximum stellar mass of the companion merging galaxy (Rodriguez-Gomez et al. 2015).

This correlation between mass in the ICL and the assembly history of the system is consistent with being an extension into the larger mass regime of the trend found for stellar haloes in MW-like galaxies (e.g. Elias et al. 2018) and is also in agreement with findings in other simulations of MW-like and groups and cluster systems using the Horizon-AGN simulations Cañas et al. (2020). Similarly, several observational studies at low and intermediate redshift find a consistent pattern where higher ICL fractions are common in systems undergoing active mergers while lower fractions are characteristic in more passive or relaxed objects (Jiménez-Teja et al. 2018, 2019b, 2021; Dupke et al. 2022; de Oliveira, Jiménez-Teja & Dupke 2022).

On the right panel of Fig. 2, we explore how TNG50 predictions compare to available theoretical and observational constraints to validate our systems. On the theoretical side, our results seem to agree, within the dispersion at a given mass, with semi-analytical models from Contini et al. (2013; shaded orange) and *N*-body + stellar tagging simulations of Rudick et al. (2011; shaded cyan).

Our results seem to also agree well with several observational constraints available in the literature (symbols with error bars), in particular, bearing in mind that the definition of ICL, band-width, and depth of the observational data varies from system to system. We discuss in more detail the compilation of individual measurements in Appendix D and also summarize the information in Table D1.

Most observational constraints seem to suggest that the ICL has less than ∼ 30 per cent of the light of the BCG, in good agreement with our results. Only NGC 5018 (red diamond), HCG 79 (highest purple triangle) and the Fornax cluster (pink triangle) have $f_{\rm ICL} > 0.3$. While in general we do not reproduce such large ICL fractions in our simulated systems, two of our groups have $f_{\rm ICL} \geq 0.3$. A careful look into the formation history of these systems (with FoF group IDs 4 and 12 in TNG50) revealed that their large ICL fractions can be attributed to two different factors. Group 4 presents a central galaxy that is under-massive compared to what is expected of its virial halo mass, such that when computing the ICL fraction it appears larger than other systems. Closer inspection revealed that this group had a rather late major merger (time ∼12.3 Gyr) that significantly increased its total mass but has not yet propagated into the central galaxy yet. Reassuringly, this group has several large-mass satellites that presumably will merge soon with the central bringing its mass into agreement with its halo mass, at which point we expect $f_{\rm ICL}$ to align with the lower values found in the sample. The second group, FoF group 12, is currently undergoing a major merger with a large satellite companion and the stripped material of this interaction is actively increasing the ICL mass without contributing yet to the central galaxy. Both of these examples are expected to decrease their $f_{\rm ICL}$ after the current interactions are settled.

Our analysis of the groups in TNG50 also revealed the presence of a substantial *in situ* stellar component within the ICL, in agreement with previous studies of stellar haloes in the predecessor Illustris simulation (D’Souza & Bell 2018; Elias et al. 2018) for smaller mass systems and a more recent study of cluster mass haloes using TNG300 simulation by Montenegro-Taborda et al. 2023 (see subsection 2.3 for a description of the *in situ* definition). We highlight in Fig. 2 where the ICL fraction would fall if one only considers the accreted component (grey-filled circles), indicating that the inclusion or not of this component does not strongly modify our results. A more detailed study of the *in situ* ICL is deferred to Ahvazi et al. (2024). In what follows, we include only the accreted component of the ICL in the analysis, unless otherwise stated.

3.2 ICL radial extent

The physical radius at which the density profile of the ICL reaches a given surface brightness limit is an observable that may help constrain theoretical models on the formation of galaxies and their associated diffuse stellar component. In order to establish a fair comparison between observations and simulations, we randomly project our simulated groups and clusters generating their 2D surface brightness maps. Following Rich et al. (2019), we measure the radius at which the surface brightness reaches 28 mag arcsec^{-2} in the r-band, using the available stellar particle magnitudes from TNG50.

We characterize the radial extension of the ICL in our simulated systems by defining two different radii, R_{28} and a_{28}, an ellipsoid-base and a circle-based definition following common practice in the field. First, we measure the average surface brightness in circular bins and find the (circular) radius R_{28} where the surface brightness is closest to 28 mag arcsec^{-2}. Secondly, we measure the surface brightness map with a 3 × 3 kpc resolution and fit an ellipse to the regions of this map exhibiting a surface brightness of 28 mag arcsec^{-2} (excluding any low-surface brightness features that may result from interactions of subhaloes). The semimajor axis of this ellipse was then used as a proxy of radial extension (a_{28}). Note that, on average, this surface brightness limit is predicted to occur at $\sim [0.2 - 0.3]\mathrm{r}_{200}$ in our systems, extending significantly beyond the central galaxy. Later generation surveys using *Euclid* or *JWST* are expected to reach several magnitudes fainter, mapping further out regions at $\sim [0.3 - 0.9]\mathrm{r}_{200}$ (see fig. C1 in Appendix C).

Fig. 3 shows the size of our simulated systems as a function of the stellar mass of the central (top panel) and the virial radius of the group (bottom panel). As expected, the elliptical semimajor axis tends to be slightly larger than the circularly averaged radius R_{28}, but they both trace similar trends. The ICL size follows a power-law relation with the mass of the central galaxy, consistent with observational constraints available at the low-mass end of our sample.

The top panel of Fig. 3 shows this good agreement by including observational results for the stellar halo of galaxies in the HERON survey (Rich et al. 2019) (magenta, purple, and grey symbols) and also the fit provided in Muñoz-Mateos et al. (2015) (grey-dashed line). Our sample, while in agreement in the low-mass end, seems to predict a slightly steeper increase in size with stellar mass for the highest mass objects than expected from the grey-dashed line.

The bottom panel of Fig. 3 indicates that the size of the ICL also shows a good correlation with the virial radius of the system, although with significant scatter. The grey- and cyan-dashed lines are best fit linear relations (y = a + b x) between the logarithmic sizes of the ICL and the haloes, characterized by the parameters a and b. For the elliptical radius a_{28}, we find the parameter values to be $a = -1.57$ and $b = 1.41$ with rms scatter of $\sim$0.1 dex, while for the circular radius R_{28}, the values are $a = -1.81$ and $b = 1.45$ with a scatter measured to be $\sim$0.1 dex. The existence of a correlation between the radial extension of the ICL and the virial radius of the host halo demonstrates that the assembly of these two components is intertwined and reaffirms the validity of the ICL as observational tracer of the distribution of dark matter in these objects.

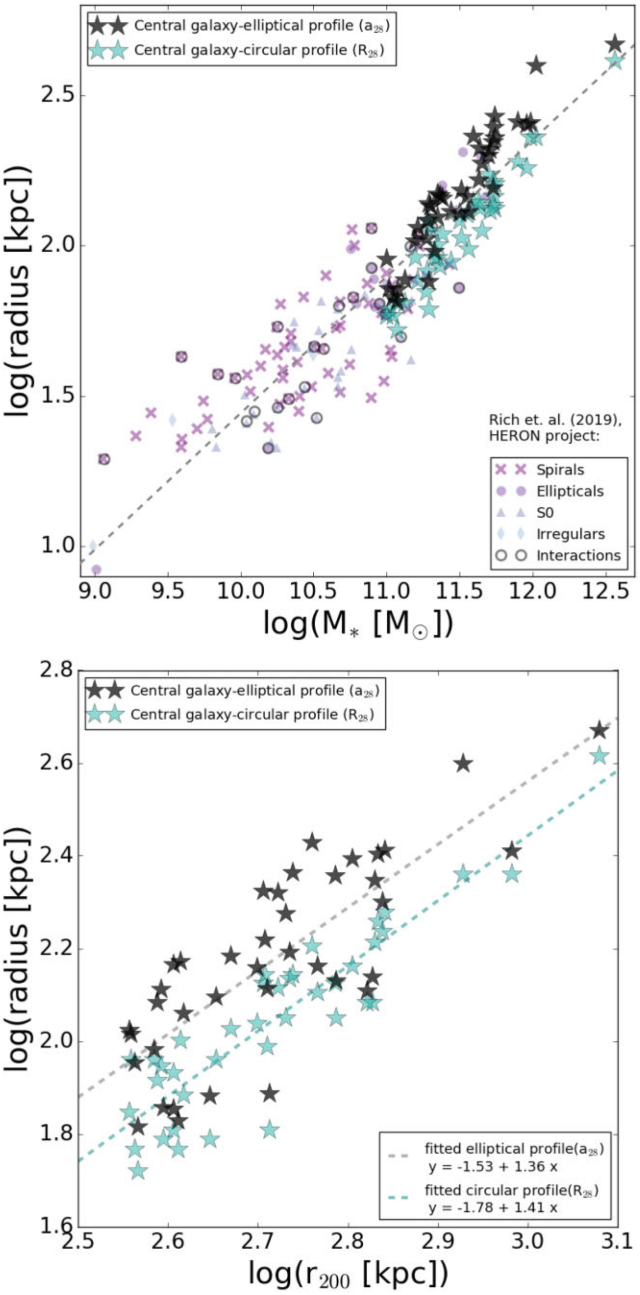

Figure 3. Size of the extended stellar halo measured by fitting ellipses to the surface brightness maps (black stars), and by measuring radius from radial binning of surface brightness maps (turquoise stars). Upper panel: Size–stellar mass relation, compared to observations from Rich et al. (2019) (coloured markers) and relation from Muñoz-Mateos et al. (2015) (grey-dashed line). Lower panel: Size as a function of virial radius of the group. Grey and turquoise dashed lines correspond to measurements of semimajor axis of the best fit ellipse and radius of the circular profile, respectively.

4 THE PROGENITORS OF THE ICL IN GROUPS AND CLUSTERS

A myriad of disrupted satellites are expected to contribute to the build up of the ICL as a consequence of the hierarchical formation scenario, making it a unique probe of the particular assembly history of a given object. Yet, while the individual formation histories may vary from halo to halo, common trends arise that may be used to

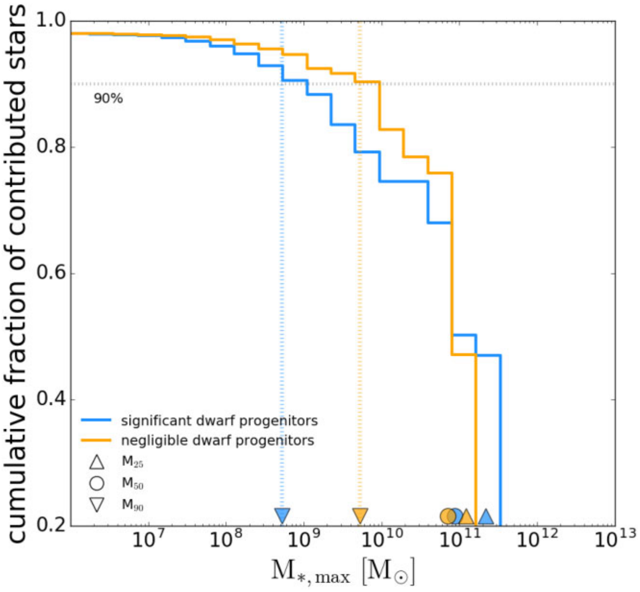

Figure 4. Example of two groups with different ICL progenitor mass functions. The vertical axis shows the cumulative fraction of stellar mass deposited in the ICL (the accreted stellar component) by galaxies with maximum stellar mass > $M_{*,\mathrm{max}}$. Markers on the *x*-axis correspond to the measured M_{25} (triangle), M_{50} (circle), and M_{90} (pointing down triangle), and horizontal and vertical lines correspond to the measurement of the M_{90} for the groups highlighted here. The group in orange has an ICL contributed mostly by massive progenitors with $M_{*,\mathrm{max}} \sim 10^{10}$ $M_\odot$ while the one in blue has significant contributions from lower mass dwarf galaxies with $M_{*,\mathrm{max}} \sim 5 \times 10^8$ $M_\odot$, as shown by their different M_{90} values.

infer details of the formation and assembly of a given object from the properties of their diffuse stellar component. For instance, in the case of MW-mass galaxies, simulations suggest that the properties of the stellar haloes are dominated by one or two most massive progenitors, which naturally explains the correlation between stellar halo mass and metallicity (e.g. Deason, Mao & Wechsler 2016; D'Souza & Bell 2018). We explore in what follows what are the typical building blocks of the ICL in more massive objects like groups and clusters, and what observational signatures may be useful to decode details of their assembly.

Fig. 4 shows the fractional contribution of stars to the ICL of two different groups (orange and blue curves) that come from progenitors of a given stellar mass $M_{*,\mathrm{max}}$. Both groups are selected to have comparable mass, $M_{200} \sim 3.2 \times 10^{13}$ $M_\odot$, but different accretion histories. Here we choose to characterize the mass of the progenitors using their maximum stellar mass $M_{*,\mathrm{max}}$, and we build the cumulative histogram of stellar particles brought in by progenitors more massive than a given $M_{*,\mathrm{max}}$. The group depicted in orange corresponds to a case where most of the mass in the ICL is contributed by relatively massive galaxies while the group shown in blue allows for significant contribution of progenitors in the regime of dwarf galaxies.

We quantify this by means of M_{25}, M_{50}, and M_{90}, which are defined as the mass of the progenitors in such cumulative distribution contributing 25 per cent, 50 per cent, and 90 per cent of the mass in the accreted ICL. For illustration, we highlight M_{90} in Fig. 4 with vertical-dotted lines and an inverted triangle, computed as the intersection of the cumulative distribution of accreted stars in each group and the 0.9 horizontal line. M_{50} and M_{25} are also denoted by a circle and a triangle for each group along the horizontal axis. The larger contribution of dwarf galaxies to the build up of the ICL in the group shown in cyan is now clearly shown by its lower mass $M_{90} = 5.2 \times 10^8$ $M_\odot$ compared to $M_{90} = 5.2 \times 10^9$ $M_\odot$ in the case of the group in orange. Differences for M_{50} and M_{25} between these two groups are smaller, but systematic.

The typical progenitors of the ICL for the full sample of groups and clusters are shown in the left panel of Fig. 5. Our results suggest that the pre-dominant contributors to their ICL are massive galaxies with $M_{50} \geq 10^{10}$ $M_\odot$, regardless of the host halo mass in this somewhat narrow M_{200} range. This is in agreement with previous

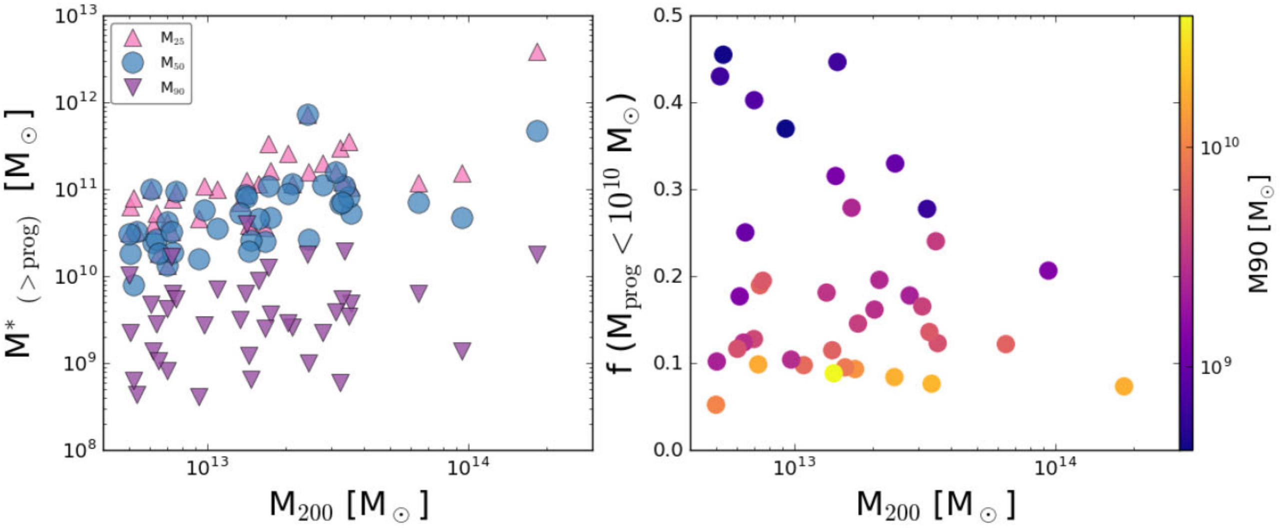

Figure 5. Left panel: Stellar mass of the progenitors that brought a percentile of accreted stellar mass to the ICL as a function of virial mass of the groups. Pink triangles, blue circles, and purple pointing down triangles correspond to M_{25}, M_{50}, and M_{90}, respectively. Note the large scatter in M_{90} indicating a varied contribution of dwarf galaxies to the build up of the ICL. Right panel: Fraction of the accreted ICL that was contributed by (dwarf) galaxies with stellar masses below $M_{*,\mathrm{max}} = 10^{10}$ $M_\odot$. Symbols are coloured by M_{90} for each group (from the left panel) and highlight the good correspondence between the two metrics. At similar halo mass, some groups have about half of their ICL built by low-mass galaxies with $M_{*,\mathrm{max}} = 10^{10}$ $M_\odot$ while others show less than 10 per cent contribution from these dwarfs.

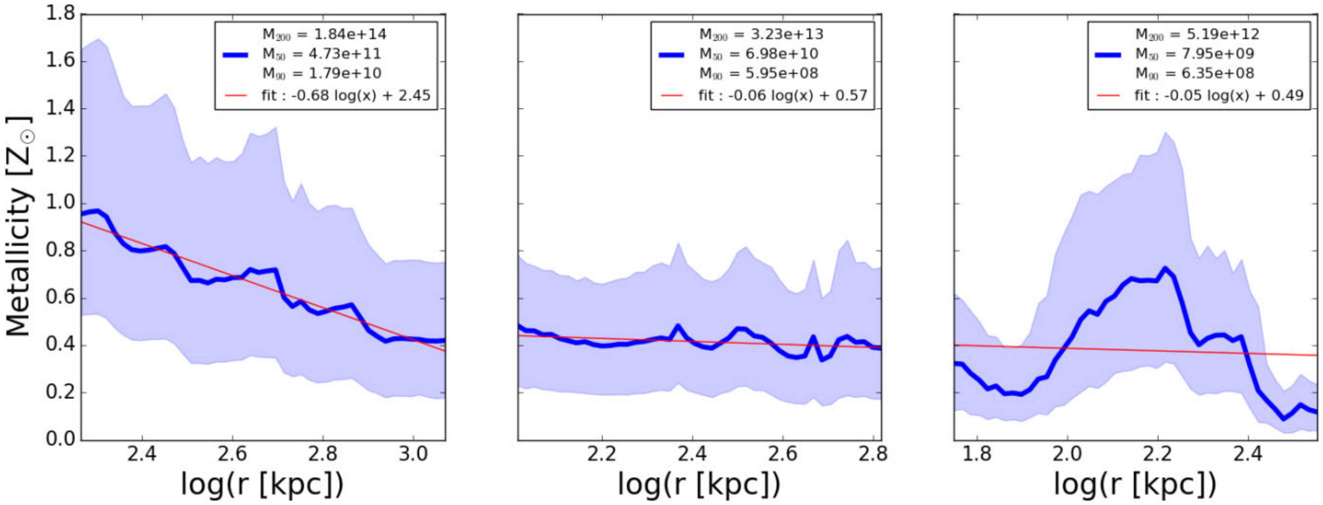

Figure 6. Illustration of the metallicity profiles for the accreted stellar component of three randomly selected groups from our sample, with the median and 25–75 percentile depicted by the blue line and shaded region, respectively. The best fit linear relation (in log) is highlighted in red and quoted in each panel. Most systems show a negative metallicity profile with radius, but the slope changes substantially from system to system.

works in the literature which identify $M_* \sim 10^{10}$–$10^{11}\,M_\odot$ as the main progenitors of the ICL in groups (e.g. Contini et al. 2013; Montes & Trujillo 2018; Contini et al. 2019; Montes et al. 2021). However, a comparison of the M_{90} values uncovers a larger variability of contributions of dwarf galaxies from halo to halo, with some systems having $M_{90} \sim 10^{10}\,M_\odot$ – and therefore having negligible mass brought in by dwarf galaxies with $M_* \sim 10^9\,M_\odot$ and below – while other systems show a more significant contribution by dwarfs with typical $M_{90} < 10^9\,M_\odot$.

This is further illustrated in the right panel of Fig. 5, which depicts the fraction of ICL mass contributed by galaxies with $M_{*,\rm max} < 10^{10}\,M_\odot$ as a function of the halo virial mass. As anticipated, these fractions can be quite different from system to system, even in the case of similar halo masses. For instance, for groups with $M_{200} \sim 10^{13}\,M_\odot$, the fraction of mass brought into the ICL by low mass galaxies with $M_{*,\rm max} < 10^{10}\,M_\odot$ varies from 10 per cent to 40 per cent, these extremes being examples of systems where dwarf galaxies play little to a significant role, respectively. Symbols in the right panel of Fig. 5 are coloured according to the previously introduced M_{90} and highlights the good correlation between both indicators: systems with a substantial contribution from low mass galaxies have a high fraction of stars brought in by progenitors with $M_{*,\rm max} < 10^{10}\,M_\odot$ and a low M_{90} value while systems built up mostly by large galaxies have a small fraction *f* and large M_{90} values.

This opens up the possibility to use different observables to attempt determine the kind of accretion history of a halo given the observed properties of their ICL. One such key observable is the metallicity profile. Fig. 6 illustrates the metallicity profile for three representative groups with differing formation histories and virial masses (as indicated by the legends). The blue curve in each panel depicts the median metallicity of the merged stellar particles in the ICL at each radius, while the blue-shaded region represents the 25th and 75th percentiles. A linear fit of the form $Z = a\log(\mathrm{r}) + \mathrm{b}$ is in general a roughly good description of our profiles (see red lines) and allow us to quantify for each object the slope of the metallicity profile (a) and its intercept (b).

Fig. 7 shows interesting correlations in the ICL observables that imprinted by the kind of progenitors that built each individual object. At a given host halo mass, systems with a larger contribution from dwarfs (blueish purple points) show less total mass in the ICL (left panel), a lower average metallicity (middle panel), and also flatter metallicity profile slopes (right-hand panel). Systems with mostly massive progenitors (yellowish orange colours) tend to show strongly declining metallicity profiles. Not shown here for brevity, the metallicity profile intercepts correlates well with the median metallicity. In all panels, points have been colour-coded by M_{90} and only the accreted component of the ICL is being considered here. However, our main results would not substantially change if, instead, we would show the total ICL (*in situ* plus accreted, grey triangles on the right panel). We have explicitly checked that similar trends exist with the stellar age profiles, with most systems displaying decreasing age profiles with radius, and some showing considerably flatter age distributions. However, ages seemed less well correlated with the assembly history of the group and cluster than the information provided by metallicity.

The ICL mass and metallicity should then be considered a valuable tool to reconstruct details on the past merger history of systems assembled within ΛCDM. Similar correlations on amount of mass, overall metallicity, and metallicity gradients with the diffuse component build-up have been found in the regime of stellar haloes for MW-like galaxies (D'Souza & Bell 2018; Monachesi et al. 2019). Our results extend upwards the range of halo masses over which these correlation are expected, including now the regime of groups and clusters.

5 TRACING THE FORMATION HISTORY OF THE ICL THROUGH GCS

We investigate how well the GCs can trace the ICL in our systems using the GC catalogue presented in Doppel et al. (2023). As detailed in subsection 2.4, we use only intra-cluster GCs (ICGCs) – GCs not gravitationally bound to any structure according to SUBFIND and that satisfy the cleaning criteria in subsection 2.2. As briefly discussed in Doppel et al. (2023), the GC tagging model predicts that the ICGC component forms via the tidal stripping of GCs from their host galaxies as they interact with their new host environment after infall. The buildup of ICGCs is thus, in a similar fashion to the ICL, a result of the hierarchical assembly of their host systems. The GC

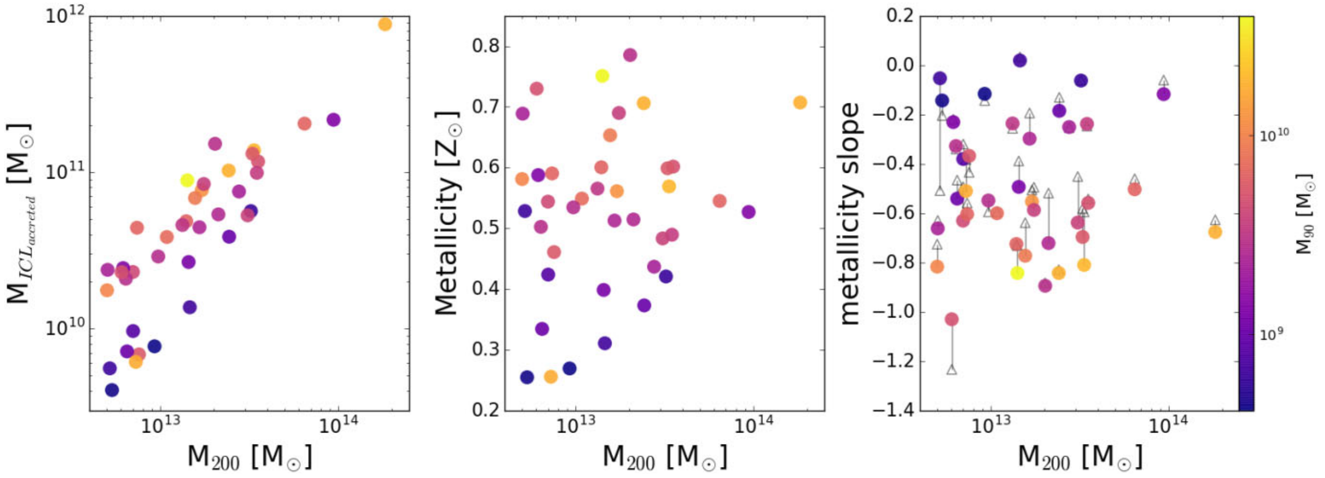

Figure 7. Left panel: Stellar mass of the accreted component in the ICL as a function of the virial mass. Middle panel: Median metallicity of the accreted stars in the ICL as a function of the virial mass. Right panel: The slope of the metallicity profile as a function of virial mass for the accreted (merged) component, with black triangles representing the results for all the stellar components (accreted + *in situ* components). All panels are colour-coded by the M_{90} of each group. Systems where dwarf galaxies play a role in building the ICL (low M_{90}) tend to have lower ICL mass, lower overall metallicity, and shallower metallicity profiles than systems with accretion dominated by more massive galaxies.

catalogue follows the population of surviving GCs with mass $M_{\rm GC} > 7 \times 10^3\,{\rm M}_\odot$, and while we do not make the distinction between ‘red’ and ‘blue’ GCs as in Doppel et al. (2023), their Fig. 5 shows that the mass density of the simulated ICGC is in good agreement with available observational constraints.

As in the case of the ICL, we find a large spread on the distribution of progenitors that build the the intra-cluster GC component in our groups. Using a similar concept to that introduced for M_{25}, M_{50}, and M_{90}, we define similar quantities but considering only the stellar mass that brought in the 25 per cent, 50 per cent, and 90 per cent of the mass in GCs in the ICGC component. Fig. 8 compares the progenitors for the ICL and the GCs. We find that GCs can be very good tracers of the most massive contributors to the ICL, in particular M_{25} and M_{50} for the stars or GCs in the diffuse component are very similar, indicating that the progenitors that build up to half of the ICL also bring along about half of the GCs in the ICGC. However, we find a clear bias in the contributors as quantified by M_{90}: taking the progenitors that bring 90 per cent of the GCs mass typically leads to smaller masses than the progenitors contributing 90 per cent of the stellar mass in the ICL (left panel Fig. 8).

This means that when using GCs to reconstruct the merger history of groups and clusters, one should keep in mind that the contribution from dwarf galaxies will be over-represented compared to the contribution of the same dwarfs to build the diffuse light component. This result can be intuitively understood from the different scaling of GCs and stellar mass with the halo mass. In the considered GC model, the mass of GCs scales as a power-law of halo mass (Doppel et al. 2023) while abundance matching results suggest a more steep decrease in the efficiency of low mass haloes to form stars compared to more massive galaxies like the MW (abundance matching is better described by a double power-law). As a result, dwarfs contribute fractionally more GCs than stars to the diffuse components. Interestingly, as found for the case of the ICL, there is a sizable range in the typical contributor of the ICGC. For some of our GC systems, M_{90} is found to be galaxies with $M_* \sim 10^{10}\,{\rm M}_\odot$, indicating little role played by low-mass galaxies. However, there are also cases with $M_{90} \sim 5 \times 10^7\,{\rm M}_\odot$, indicating dwarfs with masses typical of dSph galaxies playing a role. These differences in the accretion histories of these objects are likely to remain imprinted in the metallicity of their intra-cluster GC component and offer an avenue to constrain formation histories of massive hosts in cases where measurements of diffuse light becomes too challenging or implausible. Future GC models that are able to follow the formation and evolution of individual GC metallicities are necessary to quantify the strength of the signal expected and whether or not such signatures are to be detectable with current or future observations.

6 CONCLUSIONS

Using the cosmological hydrodynamical simulation TNG50, we have conducted a comprehensive study of two luminous tracers of dark matter in the outskirts of haloes: the ICL and the GC population. We select all groups and clusters with $M_{200} > 5 \times 10^{12}\,{\rm M}_\odot$ resulting in a sample of 39 host haloes that span the virial mass range $M_{200} = [0.5 - 20] \times 10^{13}\,{\rm M}_\odot$ and sample a wide range of formation histories. We use the catalogue of GCs tagged to the TNG50 groups and clusters presented in Doppel et al. (2023), allowing one of the first explorations of both luminous tracers in high-density environments. We focus on the study of possible imprints of these individual accretion histories on observable properties of the ICL and GCs populations. Our findings can be summarized as follows:

(i) TNG50 predictions for the fraction of light in the ICL, $f_{\rm ICL}$, are in reasonable agreement with current observational constraints for groups and low-mass clusters. In addition, $f_{\rm ICL}$ is predicted to increase with virial halo mass, albeit with significant dispersion. We find that this dispersion is well correlated with the assembly history and time of the last major merger for the BCG in our systems. Objects with more recent major mergers tend to show an excess of ICL compared to older or earlier assembled systems of comparable mass.

(ii) There is a good correlation between the radial extent of the ICL (as measured by the radius where the surface brightness profile reaches 28 mag arcsec^{-2}) and the stellar mass of the central galaxy. This size–mass scaling relation for the ICL seems to agree with the one found observationally for lower mass galaxies as part of the stellar haloes in the HERON survey (Rich et al. 2019). The radial extent of the ICL also shows a power-law relation to the virial radius

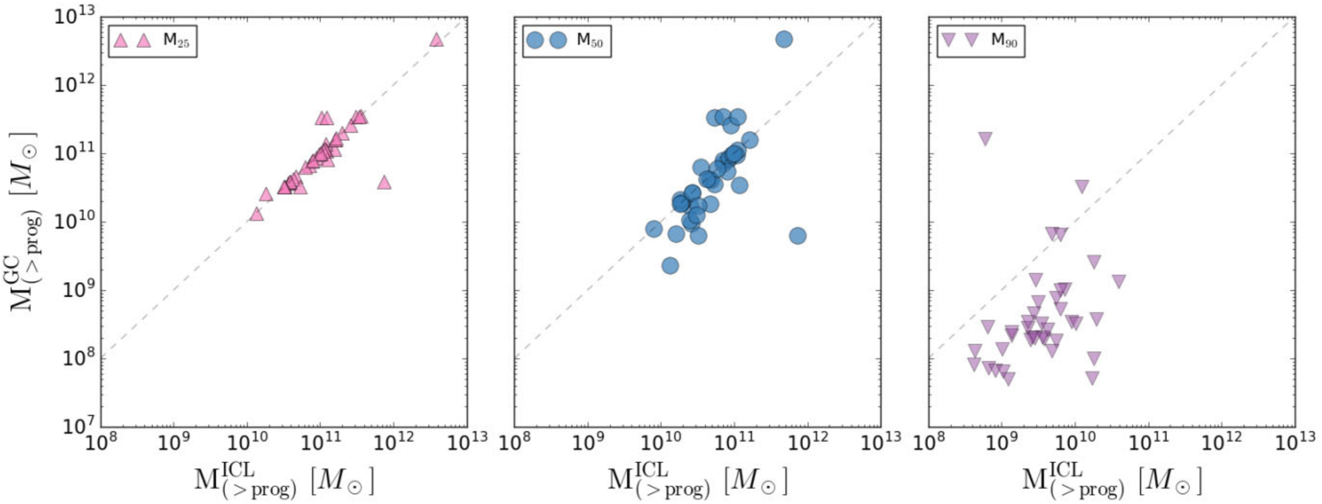

Figure 8. Typical mass of progenitors that build the ICL (*x*-axis) and the intracluster-GCs (y-axis) as quantified by M_{25} (left), M_{50} (middle), and M_{90} (right) of each population. The grey-dashed line corresponds to the one to one relation. Our findings indicate that GCs can serve as a good tracers of the most massive contributors to the ICL, although it is important to note that the contribution from dwarf galaxies may be over-represented when looking at GCs in comparison to the ICL (right panel).

of the halo, offering an observational means with which to constrain r_{200} independent of abundance matching methods. The typical rms scatter in the relation between ICL-size and virial radius is ∼0.1 dex.

(iii) The mass of the ICL is deposited by a wide range of progenitors. Some of our systems show sizable contributions from dwarf galaxies with $M* < 10^9\ \mathrm{M}_\odot$, while others are built up almost entirely by systems as or more massive than the Milky Way. We find that the average metallicity and slope of the metallicity profiles of the ICL retain information on these different assembly histories: haloes with a higher contribution from dwarf galaxies generally have shallower metallicity profiles, overall lower average metallicities and also a lower amount of mass/light in the ICL. These findings are different from the common interpretation of flat metallicity profiles as evidence of major mergers (Krick & Bernstein 2007; DeMaio et al. 2015, 2018). In our systems, the incidence of low mass galaxies is the main responsible for flattening up the *Z*-profiles. A larger role of dwarf galaxies in the build up of the ICL is also manifested by an overall lower metallicity content compared to systems built up by more massive satellite contributors.

(iv) Finally, our study highlights that ICGCs may also serve as a valuable tool to reconstruct the assembly history of the haloes. We find that lower mass dwarfs tend to make more significant contributions to the ICGC population than to the stars in the ICL, a bias that must be taken into account when reconstructing assembly histories based on metallicity of GCs or ICL. This can be understood as a consequence of the single-power-law relation of GCs with halo mass, which gives higher weight to the low mass haloes compared to the double-power-law expected for the stars in abundance matching relations.

Several of the trends studied here represent an extension of properties highlighted for the stellar haloes of galaxies like the Milky Way, including trends on amount (Pillepich et al. 2014; Elias et al. 2018), metallicity (D'Souza & Bell 2018; Monachesi et al. 2019), and radial extension (Rich et al. 2019) and their link to the assembly history of each halo. Encouragingly, the ICL in groups and clusters is more massive/brighter than in systems like the Milky Way, offering an advantage from the observational point of view to study this diffuse component. The increased sensitivity of upcoming observations with *JWST* and *Euclid* VIS Deep survey promise to reach ∼31 mag arcsec^{-2} levels in a few hours integration time. On average, for our simulated systems, this would result in detections for the ICL component all the way out to ∼0.7r_{200}, opening a new window to explore the predictions of hierarchical assembly expected for galaxies within ΛCDM.

ACKNOWLEDGEMENTS

We gratefully acknowledge the contributions of several individuals who supported this research. We would like to express our appreciation to Mireia Montes for generously providing the valuable data from (Montes 2022). We are also thankful to Nima Chartab for engaging in insightful conversations and offering valuable inputs. NA, LVS, and JED would like to acknowledge the financial support received from the NASA ATP-80NSSC20K0566, NSF-CAREER-1945310, and NSF-AST-2107993 grants.

DATA AVAILABILITY

This paper is based on halo catalogues and merger trees from the IllustrisTNG Project (Nelson et al. 2019a). These data are publicly available at https://www.tng-project.org/. The realistic GC catalogues are available to the public. They can be downloaded from: https://www.tng-project.org/doppel22.

REFERENCES

Ahvazi N., Sales L. V., Navarro J. F., Benson A., Boselli A., D'Souza R., 2024, preprint (arXiv:2403.04839)
Alamo-Martínez K. A., Blakeslee J. P., 2017, ApJ, 849, L6
Alonso Asensio I., Dalla Vecchia C., Bahé Y. M., Barnes D. J., Kay S. T., 2020, MNRAS, 494, 1859
Bijaoui A., Rué F., 1995, Signal Processing, 46, 345
Binney J., Tremaine S., 2008, Galactic Dynamics: Second Edition. Princeton Univ. Press, Princeton, NJ, USA
Borlaff A. S. et al., 2022, A&A, 657, 92
Bullock J. S., Johnston K. V., 2005, ApJ, 635, L931

Bullock J. S., Kolatt T. S., Sigad Y., Somerville R. S., Kravtsov A. V., Klypin A. A., Primack J. R., Dekel A., 2001, MNRAS, 321, 559
Cañas R., Lagos C. d. P., Elahi P. J., Power C., Welker C., Dubois Y., Pichon C., 2020, MNRAS, 494, 4314
Cattapan A. et al., 2019, ApJ, 874, L130
Conroy C., Wechsler R. H., Kravtsov A. V., 2007, ApJ, 668, L826
Contini E., 2021, Galaxies, 9, 60
Contini E., Gu Q., 2020, ApJ, 901, L128
Contini E., De Lucia G., Villalobos A., Borgani S., 2013, ApJ, 699, L1518
Contini E., Yi S. K., Kang X., 2018, MNRAS, 592, 7
Contini E., Yi S. K., Kang X., 2019, ApJ, 871, L24
Cooper A. P., Gao L., Guo Q., Frenk C. S., Jenkins A., Springel V., White S. D. M., 2015, MNRAS, 451, 2703
Cui W. et al., 2014, MNRAS, 437, 816
D'Souza R., Bell E. F., 2018, Nature Astron., 2, 737
Da Rocha C., Mendes de Oliveira C., 2005, MNRAS, 364, 1069
Da Rocha C., Ziegler B. L., Mendes de Oliveira C., 2008, MNRAS, 388, 1433
Davis M., Efstathiou G., Frenk C. S., White S. D. M., 1985, ApJ, 292, L371
DeMaio T., Gonzalez A. H., Zabludoff A., Zaritsky D., Bradač M., 2015, MNRAS, 448, 1162
DeMaio T., Gonzalez A. H., Zabludoff A., Zaritsky D., Connor T., Donahue M., Mulchaey J. S., 2018, MNRAS, 474, 3009
Deason A. J., Mao Y.-Y., Wechsler R. H., 2016, ApJ, 821, L5
Deason A. J. et al., 2020, MNRAS, 500, 4181
Dolag K., Borgani S., Murante G., Springel V., 2009, MNRAS, 399, 497
Doppel J. E. et al., 2023, MNRAS, 518, 2453
Dupke R. A. et al., 2022, ApJ, 936, L59
Durrell P. R. et al., 2014, ApJ, 794, L103
Elias L. M., Sales L. V., Creasey P., Cooper M. C., Bullock J. S., Rich R. M., Hernquist L., 2018, MNRAS, 479, 4004
Ellien A. et al., 2021, A&A, 649, 38
Engler C. et al., 2021, MNRAS, 507, 4211
Genel S. et al., 2014, MNRAS, 445, 175
Genel S. et al., 2018, MNRAS, 474, 3976
Gonzalez A. H., George T., Connor T., Deason A., Donahue M., Montes M., Zabludoff A. I., Zaritsky D., 2021, MNRAS, 507, 963
Gratton R., Bragaglia A., Carretta E., D'Orazi V., Lucatello S., Sollima A., 2019, A&AR, 27, 1
Gu M. et al., 2020, ApJ, 894, L32
Harris W. E., Reina-Campos M., 2023, MNRAS, 526, 2696
Harris W. E., Harris G. L. H., Alessi M., 2013, ApJ, 772, L82
Harris W. E., Harris G. L., Hudson M. J., 2015, ApJ, 806, L36
Harris W. E. et al., 2020, ApJ, 890, L105
Hernquist L., 1990, ApJ, 356, L359
Hudson M. J., Harris G. L., Harris W. E., 2014, ApJ, 787, L5
Hudson M. J. et al., 2015, MNRAS, 447, 298
Iodice E. et al., 2020, A&A, 635, 3
Jiménez-Teja Y., Dupke R., 2016, ApJ, 820, L49
Jiménez-Teja Y. et al., 2018, ApJ, 857, L79
Jiménez-Teja Y. et al., 2019a, A&A, 622, 183
Jiménez-Teja Y. et al., 2019b, A&A, 622, 183
Jiménez-Teja Y., Vílchez J. M., Dupke R. A., Lopes P. A. A., de Oliveira N. O. L., Coe D., 2021, ApJ, 922, L268
Jordan A. et al., 2007, ApJS, 171, 101
Ko Y. et al., 2017, ApJ, 835, L212
Krick J. E., Bernstein R. A., 2007, AJ, 134, 466
Lee M. G., Park H. S., Hwang H. S., 2010, Science, 328, 334
Lokas E. L., Mamon G. A., 2001, MNRAS, 321, 155
Longobardi A. et al., 2018, ApJ, 864, L36
Madrid J. P., O'Neill C. R., Gagliano A. T., Marvil J. R., 2018, ApJ, 867, L144
Marinacci F. et al., 2018, MNRAS, 480, 5113
McGee S. L., Balogh M. L., 2010, MNRASL, 403, 79
Melnick J., Giraud E., Toledo I., Selman F., Quintana H., 2012, MNRAS, 427, 850
Merritt A., van Dokkum P., Abraham R., Zhang J., 2016, ApJ, 830, L62
Mihos J. C., Harding P., Feldmeier J. J., Rudick C., Janowiecki S., Morrison H., Slater C., Watkins A., 2017, ApJ, 834, L16
Monachesi A. et al., 2019, MNRAS, 485, 2589
Montenegro-Taborda D., Rodriguez-Gomez V., Pillepich A., Avila-Reese V., Sales L. V., Rodríguez-Puebla A., Hernquist L., 2023, MNRAS, 521, 800
Montes M., 2022, Nature Astron., 6, 308
Montes M., Trujillo I., 2014, ApJ, 794, L137
Montes M., Trujillo I., 2018, MNRAS, 474, 917
Montes M., Trujillo I., 2019, MNRAS, 482, 2838
Montes M., Trujillo I., 2022, ApJ, 940, L51
Montes M., Brough S., Owers M. S., Santucci G., 2021, ApJ, 910, L45
Morishita T., Abramson L. E., Treu T., Schmidt K. B., Vulcani B., Wang X., 2017, ApJ, 846, L139
Muñoz-Mateos J. C. et al., 2015, ApJS, 219, 3
Murante G., Giovalli M., Gerhard O., Arnaboldi M., Borgani S., Dolag K., 2007, MNRAS, 377, 2
Naiman J. P. et al., 2018, MNRAS, 477, 1206
Navarro J. F., Frenk C. S., White S. D. M., 1996, ApJ, 462, L563
Nelson D. et al., 2015, Astronomy and Computing, 13, 12
Nelson D. et al., 2018, MNRAS, 475, 624
Nelson D. et al., 2019a, Computational Astrophysics and Cosmology, 6, 2
Nelson D. et al., 2019b, MNRAS, 490, 3234
de Oliveira N. O. L., Jiménez-Teja Y., Dupke R., 2022, MNRAS, 512, 1916
Pillepich A. et al., 2014, MNRAS, 444, 237
Pillepich A. et al., 2018a, MNRAS, 473, 4077
Pillepich A. et al., 2018b, MNRAS, 475, 648
Pillepich A. et al., 2019, MNRAS, 490, 3196
Planck Collaboration et al., 2016, A&A, 594, 13
Poliakov D., Mosenkov A. V., Brosch N., Koriski S., Rich R. M., 2021, MNRAS, 503, 6059
Puchwein E., Springel V., Sijacki D., Dolag K., 2010, MNRAS, 447, no
Purcell C. W., Bullock J. S., Zentner A. R., 2007, ApJ, 666, L20
Ragusa R. et al., 2021, A&A, 651, 39
Ragusa R. et al., 2023, A&A, 670, 20
Ramos-Almendares F., Sales L. V., Abadi M. G., Doppel J. E., Muriel H., Peng E. W., 2020, MNRAS, 493, 5357
Rich R. M. et al., 2019, MNRAS, 490, 1539
Rodriguez-Gomez V. et al., 2015, MNRAS, 449, 49
Rodriguez-Gomez V. et al., 2016, MNRAS, 458, 2371
Rudick C. S., Mihos J. C., McBride C., 2006, ApJ, 648, L936
Rudick C. S., Christopher Mihos J., Frey L. H., McBride C. K., 2009, ApJ, 699, L1518
Rudick C. S., Mihos J. C., McBride C. K., 2011, ApJ, 732, L48
Schauer A. T. P., Bromm V., Boylan-Kolchin M., Glover S. C. O., Klessen R. S., 2021, ApJ, 922, L193
Schuberth Y., Richtler T., Bassino L., Hilker M., 2008, A&A, 477, 9
Spavone M. et al., 2018, ApJ, 864, 149
Spavone M. et al., 2020, A&A, 639, 14
Spitler L. R., Forbes D. A., 2009, MNRAS, 392, 1
Springel V., 2010, MNRAS, 401, 791
Springel V., White S. D. M., Tormen G., Kauffmann G., 2001, MNRAS, 328, 726
Springel V. et al., 2018, MNRAS, 475, 676
Taylor M. A., Puzia T. H., Muñoz R. P., Mieske S., Lançon A., Zhang H., Eigenthaler P., Bovill M. S., 2017, MNRAS, 469, 3444
Vázquez-Mata J. A. et al., 2020, MNRAS, 499, 631
Vogelsberger M., Genel S., Sijacki D., Torrey P., Springel V., Hernquist L., 2013, MNRAS, 436, 3031
Vogelsberger M. et al., 2014a, MNRAS, 444, 1518
Vogelsberger M. et al., 2014b, Nature, 509, 177
Weinberger R. et al., 2017, MNRAS, 465, 3291
Weinmann S. M., Lisker T., Guo Q., Meyer H. T., Janz J., 2011, MNRAS, 416, 1197
White S. D. M., Rees M. J., 1978, MNRAS, 183, 341
Williams B. F. et al., 2007, ApJ, 656, 756
Yahagi H., Bekki K., 2005, MNRASL, 364, 86

Zibetti S., White S. D. M., Schneider D. P., Brinkmann J., 2005, MNRAS, 358, 949
Zwicky F., 1937, ApJ, 86, L217
Zwicky F., 1951, PASP, 63, 61
Zwicky F., 1952, PASP, 64, 242
Zwicky F., 1957, PASP, 69, 518

APPENDIX A: EFFECT OF ICL DEFINITION

As mentioned in subsection 3.1 there are various definitions of ICL in the literature. Here, we examine the effect on the predicted ICL mass of adopting a few of these different definitions. The methods used to define ICL are as follows; considering stellar particles that do not belong to any subhaloes in the range $0.15 \times \mathrm{r}_{200} < \mathrm{r} < \mathrm{r}_{200}$ (shown by blue circles), compared to stars in $5 \times \mathrm{r}_{\mathrm{h}_*} < \mathrm{r} < \mathrm{r}_{200}$ where $\mathrm{r}_{\mathrm{h}_*}$ is the stellar half-mass radius of the central galaxy (shown by green circles), and stars in range $\mathrm{r}_{25} < \mathrm{r} < \mathrm{r}_{200}$ where r_{25} is the radius where the surface brightness (SB) reaches 25 mag arcsec^{-2} (results are shown by orange circles). The upper-right panel of Fig. A1 shows the mass in the ICL, while the upper-left panel shows ICL fraction as a function of virial mass of the group for our sample of 39 haloes in TNG50. The lower panels show the same quantities compared to the definition of ICL used in this paper.

Our results suggest that, given the dispersion in the predicted ICL amount at a given virial mass, the changes in the definition will not significantly affect the results. All predicted fractions remain within approximately a factor of ~2 of our adopted definition, with the SB-cut-based definition consistently yielding lower values, while the $5 \times \mathrm{r}_{\mathrm{h}_*} < \mathrm{r} < \mathrm{r}_{200}$ definition tends to predict higher fractions than our adopted one.

APPENDIX B: THE GC TAGGING TECHNIQUE

Below is a summary of the method introduced in Doppel et al. (2023) to tag GCs into the TNG50 simulations. We add GC particles to all selected galaxies in TNG50 that interact with the 39 most massive groups ($M_{200} > 5 \times 10^{12}$ M$_\odot$). The procedure is done at their time of infall, when we select the full set of DM particles that follow a given energy distribution. The energy distribution is calculated by assuming that the DM haloes of the selected galaxies conform to an NFW profile (Navarro, Frenk & White 1996):

$$\rho_{\mathrm{NFW}}(r) = \frac{\rho^0_{\mathrm{NFW}}}{(r/r_{\mathrm{NFW}})(1 + r/r_{\mathrm{NFW}})^2}, \tag{B1}$$

that is fit to each galaxy at infall following Lokas & Mamon (2001). We assume a scale radius, $\mathrm{r}_{\mathrm{NFW}} = \mathrm{r}_{\max}/\alpha$ where $\mathrm{r}_{\max}$ is the radius of

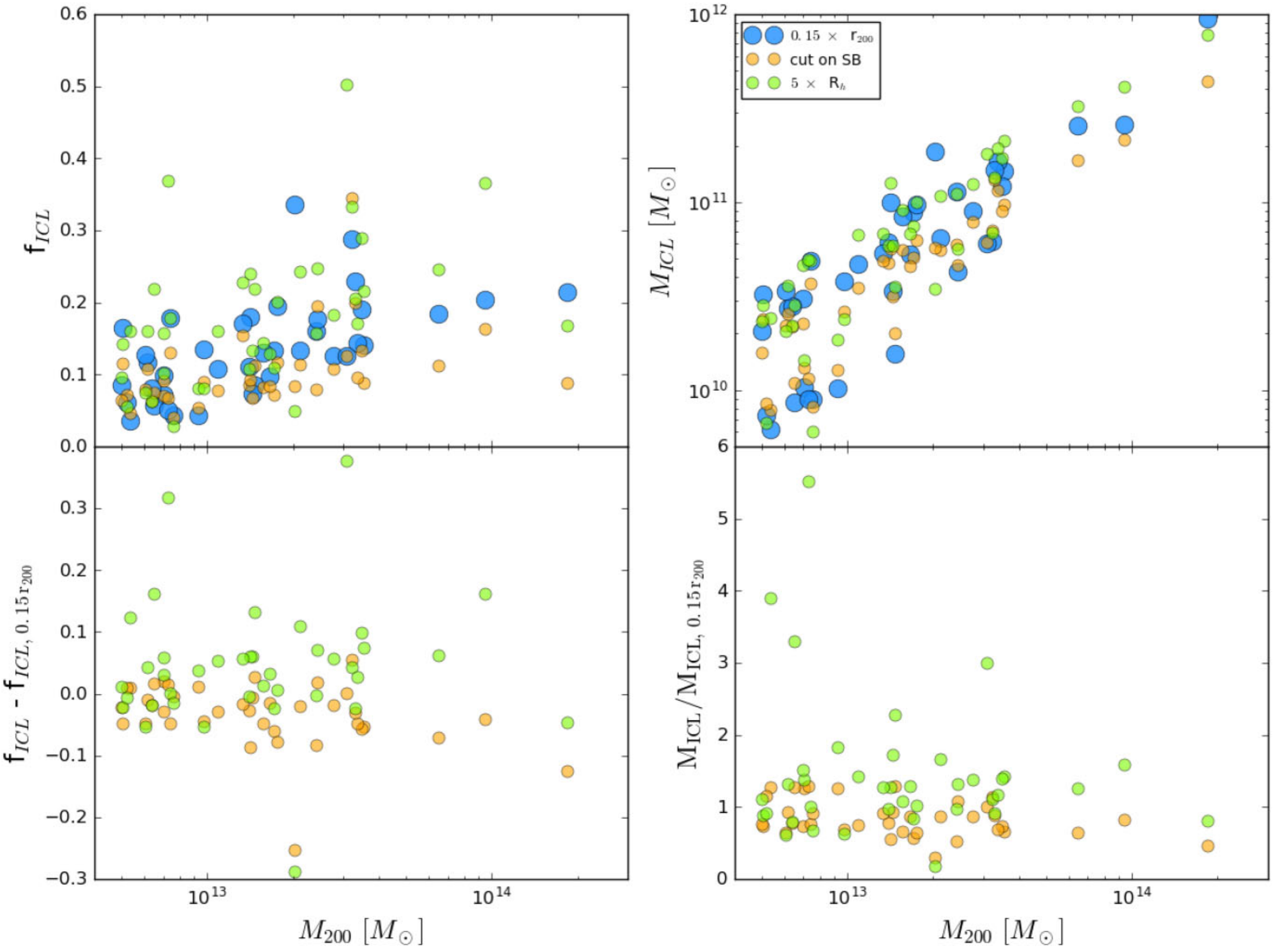

Figure A1. Upper left panel: ICL fraction as a function of virial mass. Upper right panel: Stellar mass content in the ICL as a function of virial mass. Lower left panel: Alternative ICL fractions compared to the method used in this paper. Lower right panel: The fraction of stellar mass content in the ICL measured from alternative definitions to the mass content from the ICL definition method used in this paper. The different colours correspond to various definitions of ICL.

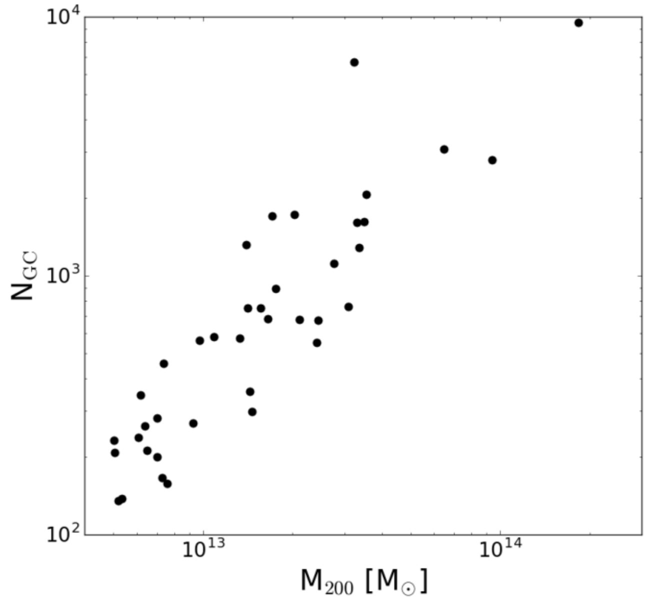

Figure B1. Number of GCs in the ICL as a function of the virial mass of the haloes.

maximum circular velocity calculated from the dark matter particle distribution in the simulation and $\alpha = 2.1623$ (Bullock et al. 2001).

Subsequently, GCs are assumed to follow a Hernquist profile (Hernquist 1990):

$$\rho_{\rm HQ}(r) = \frac{\rho^0_{\rm HQ}}{(r/r_{\rm HQ})(1 + r/r_{\rm HQ})^3}. \tag{B2}$$

with scale radius $r_{\rm HQ}$ is dependent upon whether the GC is "red" or "blue". The "red" component is intended to be representative of a more radially concentrated metal-rich GCs, while a "blue" component refers to a more radially extended and metal-poor population of GCs. Following (Ramos-Almendares et al. 2020), it is assumed that $r_{\rm HQ} = \beta r_{\rm NFW}$, where $\beta_{\rm red} = 0.5$ and $\beta_{\rm blue} = 3.0$. $\rho_{\rm HQ}$ is fit such that the number of GC candidates are maximized.

Further, the distribution function is calculated for the NFW halo, the blue GCs, and the red GCs following Binney & Tremaine (2008):

$$f_i(\epsilon) = \frac{1}{8\pi}\left[\int_0^{\epsilon} \frac{{\rm d}^2\rho_{\rm i}}{{\rm d}\psi^2}\frac{{\rm d}\psi}{\sqrt{\epsilon-\psi}} + \frac{1}{\sqrt{\epsilon}}\left(\frac{{\rm d}\rho_{\rm i}}{{\rm d}\psi}\right)\bigg|_{\psi=0}\right], \tag{B3}$$

where ρ_i is the density profile of i = (DM, red GCs, blue GCs), Ψ is the relative gravitational potential, and ϵ is the relative energy. In bins of relative energy, a fraction $\rm f_{HQ,i}/f_{DM}$ of the DM particles are selected to be GCs, and the final set of GC candidates are defined to be within a cutoff radius of $\rm r_h/3$, where $\rm r_h$ is the total half-mass radius of the galaxy, following Yahagi & Bekki (2005).

The method assumes a power-law relation between the total GC mass and the halo mass of each galaxy whose normalization is calibrated such that it reproduces the observed relation at the present-day (Harris et al. 2015). Only haloes with $M_{200} > 10^{11}$ $\rm M_\odot$ participate in the calibration process and properties of lower mass objects can be considered a prediction. More specifically, the resulting coefficients for the M_{GC} - $\rm M_{halo}$ relation at infall are

$$M_{{\rm GC},z=0} = a M^b_{{\rm halo},z=0}, \tag{B4}$$

where $\rm a = 2.6 \times 10^{-8}$ and 4.9×10^{-5} for red and blue GCs, respectively, with b = 1.2 and 0.96 for red and blue GCs. Similarly to Harris et al. (2015), z = 0 halo masses are calculated assuming abundance matching parameters from Hudson et al. (2015).

The calibration for GC mass is made using the amount of GC stripping by z = 0: $\rm f_{bound} = N_{candidates,z=0}/N_{candidates,infall}$. Where a GC candidate is considered (still) bound to a galaxy if its corresponding DM particles are identified as part of the galaxy via `SUBFIND`. Assuming that at infall, the relation between $\rm M_{GC}$ and $\rm M_{halo}$ still follows a power law

$$M_{\rm GC,inf} = \frac{1}{f_{\rm bound}} M_{{\rm GC},z=0} = a_{\rm inf} M^{b_{\rm inf}}_{\rm halo,inf}, \tag{B5}$$

with the coefficient and exponent found to be $\rm a_{inf} = 2.6 \times 10^{-7}$ and 7.3×10^{-5} and $b_{\rm inf} = 1.14$ and 0.98 for red and blue GCs, respectively.

Finally, the number of all identified GC candidates with energy consistent with the distribution of red and blue GCs is in most cases larger than the observed number of GCs around such galaxies. Subsequently, the GC candidates at infall for each galaxy are subsampled to obtain a realistic number of GCs (Fig. B1 shows the number of GCs in the ICL for our sample of groups and clusters). For a given galaxy, we assume that the z-band luminosity function of GCs is Gaussian, centred on $L_{GC} = 2 \times 10^5$ $\rm L_\odot$ with a dispersion that varies with galaxy luminosity (as found by Jordan et al. 2007). We select GC luminosities, converting them to masses assuming a z-band mass to light ratio of 1 $\rm M_\odot/L_\odot$, until the total selected mass in GCs is consistent with the total GC mass assigned to the galaxy at infall. The resulting individual GC masses, $\rm m_{GC}$ are in the range 7×10^3 $\rm M_\odot \le m_{GC} \le 5 \times 10^6$ $\rm M_\odot$, consistent with observational constraints from Jordan et al. (2007).

APPENDIX C: SURFACE BRIGHTNESS PROFILES

In order to establish a fair comparison between observations and simulations, we randomly project our simulated groups and clusters

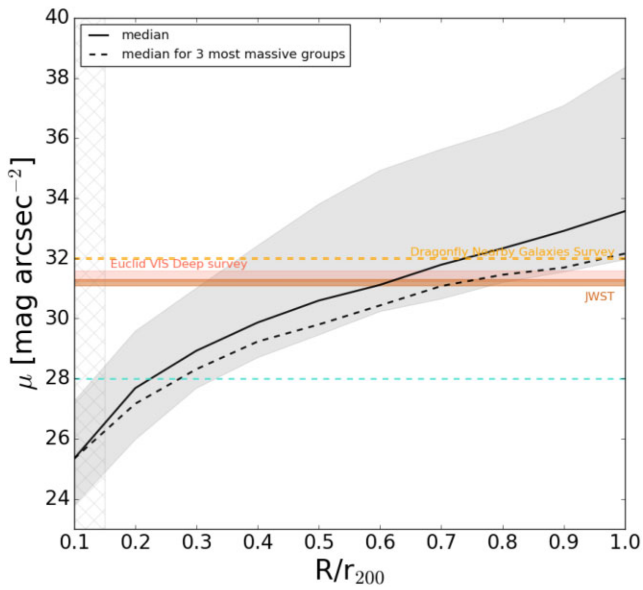

Figure C1. Surface brightness profiles of our sample of groups and clusters. The black line represents the median profile for the entire sample, while the dashed-black line corresponds to the median profile of the three most massive groups. The shaded region illustrates the dispersion across all groups in our sample. The grey-hatched region indicates the extent of the BCG.

generating their 2D surface brightness maps. The results are presented in Fig. C1, where the solid-black line represents the median surface brightness for our entire sample in circular radii bins. Because we span a range of host halo masses, we normalize the horizontal axis to the virial radius of each system. The shaded grey region illustrates the whole range of surface brightness covered by our entire sample. This variation in profile is given by two factors: object-to-object differences in assembly history and mass in the ICL and, also important, the range of host halo masses being included. For illustration, the median surface brightness including only the three most massive clusters with $M_{200} \sim 10^{14}\,\mathrm{M}_{\odot}$ is shown by the dashed-black line, which is systematically ∼1 magnitude brighter that considering the whole sample. The area being shaded by hatching for $R/r_{200} < 0.15$ separates the inner regions attributed to the BCG and not considered part of the ICL.

The turquoise horizontal dashed line indicates the 28 mag arcsec^{-2} limit at which we measure the radius of each group. For comparison, we have included estimates of the surface brightness limits for the *JWST* (based on the study of ICL in SMACS 0723 by Montes & Trujillo 2022[3]), the Euclide VIS Deep survey (Borlaff et al. 2022)[1], and the Dragonfly Telephoto Array's deep nearby galaxy survey (which provides g-band surface brightness profiles down to 31–32 mag arcsec^{-2}, see Merritt et al. (2016) for applications to stellar halo studies). We predict that observational campaigns in the future targeting ∼31 mag arcsec^{-2} are a promising avenue to map the stellar diffuse component in groups and clusters out to at least half the virial radius.

APPENDIX D: SUMMARY OF OBSERVATIONS

In this section, we present the observational data utilized for the ICL fraction–halo mass relation. Although efforts were made to gather data from sources employing consistent definitions and methods, some studies included in this compilation used different techniques to identify the ICL. For instance, Spavone et al. (2020) studied the Fornax cluster and utilized multicomponent fits[4] to distinguish the ICL component, revealing that approximately 34 per cent of the total light in this cluster originates from the ICL. Another study by Da Rocha & Mendes de Oliveira (2005); Da Rocha et al. (2008) employed wavelet techniques[5] to measure the ICL in six objects from the Hickson Compact Group (HCG) catalogue, resulting in a wide range of observed ICL fractions. The ICL fractions varied from no detected ICL in HCG 88 to approximately 33 per cent for HCG 79 (the fraction representing the ratio of ICL light to the total light of the group in the R band). Some studies have combined observational results with semi-analytical simulations to estimate the ICL fraction, such as the deep survey of the Virgo cluster conducted by Mihos et al. (2017), which estimated a range of 7–15 per cent for the ICL fraction.

Furthermore, variations in the choice of observational bands used to infer the ICL fraction can be noticed. Different bands can yield different measurements of the ICL fraction. For example, Ragusa et al. (2021) investigated HCG 86 and found an ICL fraction of 14 per cent in the r band and 19 per cent in the g band, highlighting how the choice of band in observations can influence the measured amount of light attributed to the ICL.

An interesting outcome of these measurements is the dispersion observed in the ICL fraction at a given halo mass. Iodice et al. (2020) compared the ICL fractions of several different objects using the same method and demonstrated how features present in the ICL, outer envelope of the brightest cluster galaxy, and the presence of HI can indicate different evolutionary stages and mass assembly histories for different groups and clusters.

Additionally, some studies have linked the ICL fraction to the mean morphology of the group or cluster. Poliakov et al. (2021) measured the ICL fraction for multiple HCG objects and found that the mean surface brightness of the intra-group light correlates with the mean morphology of the group, with brighter intra-group light observed in groups with a larger fraction of early-type galaxies. It is important to note that the investigated groups in the TNG50 simulations exhibit various morphologies and formation histories, which may contribute to the wide variation in ICL fractions at a given mass.

Table D1 below provides a summary of the observational results compiled from multiple sources.

---

[3] These limits correspond to a sky fluctuation of 3σ in an area of 10×10 arcsec^{2}.

[4] Using multiple equations to describe BCG + ICL (such as single or double Sérsic profiles and/or exponential profiles).

[5] The wavelet technique consists of deconvolving the signal into wavelet coefficients (since images are a 2D signal, each wavelet coefficient corresponds to a plane), identifying the objects representations in the wavelet space, defining the objects with a 'multiscale vision model' (Bijaoui & Rué 1995) and reconstructing the detected objects (Da Rocha & Mendes de Oliveira 2005; Jiménez-Teja & Dupke 2016; Ellien et al. 2021).

Table D1. Observational data.

Toprule object	Reference for f_{ICL}	f_{ICL}	M_{halo} [10^{13} $\mathrm{M}_{\odot}$]	Comments
Fornax	Spavone et al. (2020)	34 per cent (21.4 per cent – 53.8 per cent)	6.3	Reference for mass: Spavone et al. (2020); Ragusa et al. (2021); Montes (2022) observation was conducted in u, g, r, i bands (Spavone et al. 2020)
	Montes (2022)	34 per cent (19 per cent – 49 per cent)		
	Ragusa et al. (2021)	34 ± 2 per cent		
Virgo	Mihos et al. (2017)	7 – 15 per cent	31.6 (1)	Reference for mass (1): Ragusa et al. (2021); Spavone et al. (2020). Reference for mass (2): Weinmann et al. (2011) observation was conducted in B and V bands (Mihos et al. 2017) Using results of simulations (Rudick et al. 2009), Mihos et al. (2017) estimated 5–10 per cent of the ICL should be the form of coherent streams (the relatively high surface brightness tidal features that represent material most recently stripped from their host galaxies), which help them estimate the whole amount of ICL luminosity.
	Ragusa et al. (2021)	11 ± 3 per cent	14–40 (2)	
IC 1459	Iodice et al. (2020); Ragusa et al. (2021)	2 ± 2 per cent	3.7	Reference for mass: Iodice et al. (2020); Ragusa et al. (2021) observation was conducted in g and r bands (Iodice et al. 2020)
NGC 5018	Spavone et al. (2018)	41 per cent	0.68	Reference for mass: Ragusa et al. (2021); Iodice et al. (2020); Montes (2022) observation was conducted in u, g, r bands (Spavone et al. 2018)
	Ragusa et al. (2021)	40 ± 5 per cent		
	Iodice et al. (2020)	41 ± 5 per cent		
NGC 1533	Ragusa et al. (2021); Iodice et al. (2020)	8 ± 2 per cent	0.49	Reference for mass: Ragusa et al. (2021); Iodice et al. (2020) observation was conducted in g, r bands (Cattapan et al. 2019)
HCG 8	Poliakov et al. (2021); Ragusa et al. (2021)	25.1 per cent	5.29	Reference for mass: Montes (2022) observation was conducted in r band (Poliakov et al. 2021)
HCG 15	Da Rocha, Ziegler & Mendes de Oliveira (2008); Iodice et al. (2020)	B: 16 ± 3 per cent $^{a, b}$ R: 18 ± 4 per cent$^{a, b}$	5.3^{b} (1)	Reference for mass (1): Da Rocha et al. (2008); Montes (2022). Reference for mass (2): Da Rocha et al. (2008); Ragusa et al. (2021); Iodice et al. (2020) observation was conducted in B and R bands (Da Rocha et al. 2008)
	Da Rocha et al. (2008); Ragusa et al. (2021)	B: 19 ± 4 per cent $^{a, c}$ R: 21 ± 4 per cent$^{a, c}$	5.67^{c} (2)	
HCG 17	Poliakov et al. (2021)	16.3 per cent		Observation was conducted in r band (Poliakov et al. 2021)
HCG 35	Da Rocha et al. (2008); Ragusa et al. (2021); Iodice et al. (2020)	B: 15 ± 3 per cent ^{a} R: 11 ± 2 per cent^{a}	1.51 (1)	Reference for mass (1): Da Rocha et al. (2008); Ragusa et al. (2021); Iodice et al. (2020); Montes (2022). Reference for mass (2): Montes (2022) observation was conducted in B and R bands (Da Rocha et al. 2008)
	Poliakov et al. (2021)	12.8 per cent	3.1 (2)	
HCG 37	Poliakov et al. (2021); Ragusa et al. (2021)	12.7 per cent	5.87 (1)	Reference for mass (1): Montes (2022). Reference for mass (2): Ragusa et al. (2021) observation was conducted in r band (Poliakov et al. 2021)
			2.24 (2)	
HCG 51	Da Rocha et al. (2008); Iodice et al. (2020)	B: 26 ± 5 per cent $^{a, b}$ R: 24 ± 5 per cent$^{a, b}$	3.59^{b} (1)	Reference for mass (1): Da Rocha et al. (2008); Montes (2022). Reference for mass (2): Da Rocha et al. (2008) observation was conducted in B and R bands (Da Rocha et al. 2008)
	Da Rocha et al. (2008); Ragusa et al. (2021)	B: 31 ± 6 per cent $^{a, c}$ R: 28 ± 5 per cent$^{a, c}$	0.74^{c} (2)	
HCG 74	Poliakov et al. (2021); Ragusa et al. (2021)	7.5 per cent	28.65	Reference for mass: Montes (2022) observation was conducted in r band (Poliakov et al. 2021)
HCG 79	Da Rocha & Mendes de Oliveira (2005); Ragusa et al. (2021)	B: 46 ± 11 per cent ^{a} R: 33 ± 11 per cent^{a}	1.04 (1)	Reference for mass (1): Montes (2022). Reference for mass (2): Ragusa et al. (2021); Iodice et al. (2020) observation was conducted in B and R bands (Da Rocha & Mendes de Oliveira 2005)
	Iodice et al. (2020)	46 ± 10 per cent	3.98 (2)	
HCG 86	Ragusa et al. (2021)	Radius $<$ 160kpc : g: 19 ± 3 per cent (35 ± 5 per cent ^{d}) r: 14 ± 2 per cent (29 ± 6 per cent ^{d}) Radius $<$ 120kpc : g:16 ± 3 per cent (28 ± 5 per cent ^{d}) r: 11 ± 2 per cent (23 ± 7 per cent ^{d})	0.85	Reference for mass: Ragusa et al. (2021) observation was conducted in g, r, i bands (Ragusa et al. 2021)
HCG 88	Da Rocha & Mendes de Oliveira (2005); Iodice et al. (2020)	0^{a}	2.88 (1)	Reference for mass (1): Montes (2022). Reference for mass (2): Iodice et al. (2020) observation was conducted in B and R bands (Da Rocha & Mendes de Oliveira 2005)
			0.12 (2)	
HCG 90	Ragusa et al. (2021); Iodice et al. (2020)	38 ± 3 per cent	1.17	Reference for mass: Ragusa et al. (2021); Iodice et al. (2020)
HCG 95	Da Rocha & Mendes de Oliveira (2005); Ragusa et al. (2021)	B: 11 ± 26 per cent ^{a} R: 12 ± 10 per cent^{a}	2.14	Reference for mass: Ragusa et al. (2021); Montes (2022) observation was conducted in B and R bands (Ragusa et al. 2021) (Poliakov et al. 2021)

[a] ICL fractions are measured using wavelet technique

[b] corresponding to sextet configuration

[c] corresponding to quintet configuration

[d] Measured ICL fraction with respect to mass of the BCG

This paper has been typeset from a TEX/LATEX file prepared by the author.